
This manuscript is a preprint and will be shortly submitted for publication to a scientific journal. As a function of the peer-reviewing process that this manuscript will undergo, its structure and content may change.

If accepted, the final version of this manuscript will be available via the 'Peer-reviewed Publication DOI' link on the right-hand side of this webpage. Please feel free to contact any of the authors; we welcome feedback.

1 **Space-time landslide size modelling in Taiwan**

2 Zhice Fang^{1,2}, Yi Wang^{1,*}, Cees van Westen², Luigi Lombardo²

3 ¹ Institute of Geophysics and Geomatics, China University of Geosciences, Wuhan
4 430074, China

5 ² University of Twente, Faculty of Geo-Information Science and Earth Observation
6 (ITC), PO Box 217, Enschede, AE 7500, Netherlands

7 *Correspondence Author: Yi Wang (wangyi@whu.edu.cn)

8

9 **Abstract**

10 Landslide susceptibility assessment using data-driven models has predominantly
11 focused on predicting where landslides may occur and not on how large they might be.
12 The spatio-temporal evaluation of landslide susceptibility has only recently been
13 addressed, as a basis for predicting where and when landslides might occur. The present
14 study combines these new developments by proposing a data-driven model capable of
15 estimating how large landslides may be, for the Taiwan territory in a fourteen year time
16 window. To solve this task, our model assumes that landslide sizes follow a Log-
17 Gaussian probability distribution in space and time. Spatially the area is subdivided into
18 46074 slope units, with 14 annual timesteps from 2004 to 2018. Based on this
19 subdivision, the model we implemented regressed landslide sizes against a covariate
20 set that includes temporally static and dynamic properties. In the validation of our
21 model, we nested a wide range of cross-validation (CV) procedures, such as a
22 randomized 10fold-CV, a spatially constrained CV, a temporal leave-one-year-out CV,
23 and a spatio-temporal CV. The final performance was described both numerically as
24 well as in map forms.

25 Overall, our space-time model achieves interpretable and satisfying results. With the

26 availability of more complete landslide inventories, both temporally and spatially, we
27 envision that spatio-temporal landslide size prediction will become the next challenge
28 for geomorphologists to finally address a fundamental component of the landslide
29 hazard definition. And, because of its spatio-temporal nature, we also envision that it
30 may lead to simulation studies for varying climate scenarios.

31 **Keywords:** dynamic landslide area prediction; space-time modelling; slope unit;
32 spatio-temporal cross-validation

33 **1. Introduction**

34 Landslides are a common natural hazard in many mountainous landscapes worldwide,
35 and a serious threat to human lives and properties (Rossi et al., 2019; Merghadi et al.,
36 2020). Therefore, accurate prediction of landslide location and size is a crucial
37 requirement for reliable hazard and subsequent risk assessment. The most generally
38 accepted definition of landslide hazard requires the estimation of three aspects: i) the
39 probability of occurrence at a given location, ii) within a specified period, and iii) with
40 a given magnitude (Varnes, 1984; Guzzetti et al., 1999; Guzzetti et al., 2005). This
41 definition essentially addresses three main questions that a decision maker requires to
42 implement any risk mitigation strategy: “where”, “how frequent”, and “how large”
43 landslides might be in a certain area. This definition was later improved by Corominas
44 et al. (2014) as they introduced the landslide intensity concept to measure the spatial
45 variation in the level of threat that landslides may carry across a landscape. However,
46 the intensity that Corominas and co-authors mainly considered consisted of dynamic
47 spatially distributed characteristics such as velocity, impact pressure or kinematic
48 energy, which are derived using physically-based models. The parameters for these
49 models are virtually impossible to collect over larger areas, due to the heterogeneity of
50 the landscape, which is the reason why recent efforts have been made towards

51 expressing landslide intensity over larger areas in terms of counts (Lombardo et al.,
52 2018) or sizes (Lombardo et al., 2021) as a basis for data-driven modelling. These
53 publication represent two examples of a long list of data-driven studies in the context
54 of landslide prediction, which were largely dedicated to purely predicting occurrence
55 locations (or susceptibility), and only recently they have branched out towards other
56 landslide characteristics. Specifically, data driven susceptibility models were initially
57 framed in a bivariate statistical structure (e.g., Van Westen et al., 2003; Nandi and
58 Shakoor, 2010), and this essentially remained the case until they were superseded by
59 their multivariate statistics counterpart (e.g., Chung et al., 1995; Atkinson and Massari,
60 1998). Only recent years have witnessed the spread of machine learning (e.g., Merghadi
61 et al., 2020) and deep learning (e.g., Fang et al., 2021; Aguilera et al., 2022)
62 architectures with improved predicting performance they ensure. These models have
63 mostly been used purely in space, with very few applications to the space-time context
64 (Lombardo et al., 2020), aside from empirical rainfall thresholds (Jaiswal et al., 2010;
65 Nefeslioglu and Gorum, 2020) or coseismic near-real time prediction (Nowicki Jessee
66 et al., 2018).

67 Specifically for statistical studies a common assumption is the choice of a suitable
68 distribution reflecting the data on landslides. For this reason, susceptibility models
69 assume a Bernoulli probability distribution (Steger et al., 2016; Steger et al., 2017),
70 whereas intensity models based on counts assume the Poisson probability distribution
71 (Lombardo et al., 2019; Opitz et al., 2022) instead. When it comes to model landslide
72 area, the choice is not straightforward. In fact, it is common that a landslide area
73 distribution is quite heavily tailed. In other words, the vast majority of inventories
74 includes a predominant number of small landslides and only few extremely large ones,
75 which is common in response to major triggering events, such as rainfall (Jones et al.,

76 2021; Emberson et al., 2022) or earthquakes (Zhang et al., 2019; Tanyaş et al., 2022).
77 This is the reason that has led Malamud et al. (2004) to propose the Inverse Gamma
78 distribution as a universal empirical size model, which lead to a series of studies on
79 landslide Frequency Area Distribution (FAD; Tanyaş et al., 2018). However, one
80 weakness of the FAD approach is that it neglects the spatial distribution of the
81 landslides it considers, something that has been recently accounted for in a few articles
82 on the subject. Specifically, Lombardo et al. (2021) and Moreno et al. (2022) were the
83 first to propose a Log-Gaussian model able to estimate the expected planimetric extent
84 of landslides over a given landscape. However, their model lacked the ability to inform
85 whether any given slope will be unstable. For this reason, Aguilera et al. (2022) and
86 Bryce et al. (2022) extended this framework by building a joint landslide susceptibility
87 and area prediction model. But even in these cases, one main issue still persisted, for
88 they produced temporally stationary estimates of landslide extents. By leaving the
89 temporal dimension unexplored, most studies neglected a crucial requirement of both
90 hazard definitions proposed by Guzzetti et al. (1999) and Corominas et al. (2014), and
91 even reported in the international guidelines for landslide risk (Fell et al., 2008). Also,
92 such stationary models may not be valid over large areas and in the context of rapid
93 climate change, because global warming can influence landslide activity, abundance,
94 and frequency (Gariano and Guzzetti, 2016). Therefore, an important research gap to
95 be addressed relates to how these purely spatial size models can be reliably extended
96 over time.

97 One way to do so based on physically-based modelling (Park et al., 2019; Van den
98 Bout et al., 2021). However, the unavailability of required geotechnical parameters
99 mostly constrains their applicability to individual slopes or small catchment analyses.
100 Data-driven approaches can by-pass the geotechnical requirements as long as a reliable

101 multi-temporal landslide inventory is available (Guzzetti et al., 2012), together with a
102 set of static and dynamic explanatory variables (Wang et al., 2021) capable of
103 explaining landslide size distribution in space and time. Based on these considerations
104 we propose a space-time landslide size model to estimate the planimetric landslide area
105 in any given mapping and temporal unit. Specifically, we present the implementation
106 of a Log-Gaussian generalized additive model (GAM), which assumes that landslide
107 size follows a log-Gaussian distribution in the space-time domain. The spatio-temporal
108 characteristics of landslide size are captured by incorporating a set of static and dynamic
109 factors. The same model is constrained to treat mapping units that are close in space to
110 behave more similarly compared to those that are far away, and the same is valid in
111 time.

112 We tested this model with a dataset of the main island of Taiwan for the period from
113 2004 to 2018, during which tropical cyclones triggered many landslides. Earlier, we
114 have implemented a space-time landslide susceptibility model for the same study area
115 (Fang et al., 2022), which focused on the landslide space-time prediction. This present
116 study aims at estimating probabilistically “how frequent” and “how large” landslides
117 are expected within mapping units. We consider this a step forward towards a new
118 generation of probabilistic landslide hazard assessment, beyond what is currently
119 available in the literature.

120 **2. Study area and data overview**

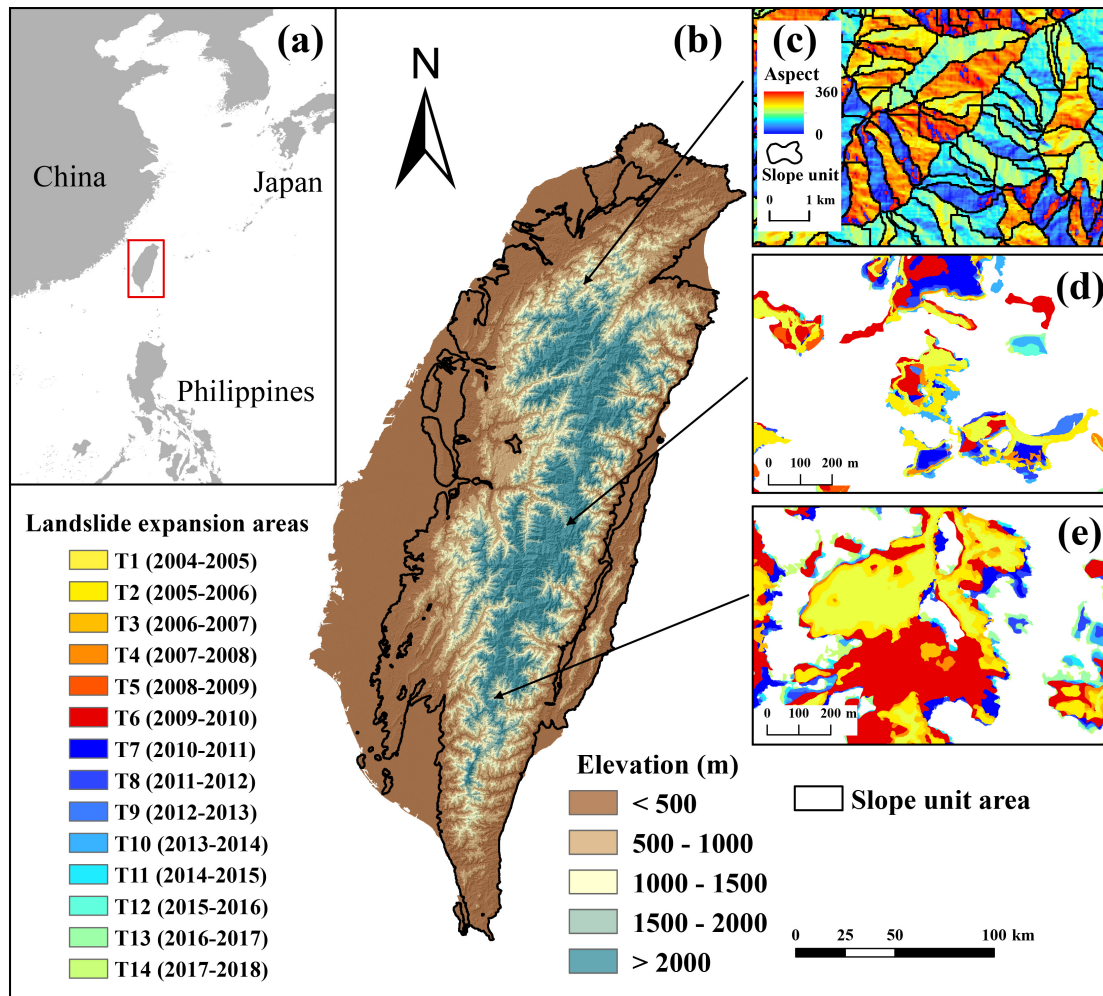
121 **2.1. Study area**

122 We implemented the space-time landslide size modelling in the same study area as
123 our previous study (Fang et al., 2022). The study area is located in the main island of
124 Taiwan (**Fig. 1**) and extends over a total of 35,808 km². Taiwan is frequently affected
125 by landslides triggered by typhoons and/or earthquakes, a unique condition owed to its

126 geographical location within the Pacific Ring of Fire and in the path of tropical cyclones.
127 For example, the 1999 Chi-Chi earthquake triggered more than 10,000 landslides in
128 central Taiwan, with a total sliding area of exceeding 100 km² (Hung, 2000). Typhoon
129 Morakot in 2009 brought an accumulated rainfall of 3059 mm and resulted in more than
130 22,705 landslides covering an total area of 274 km² (Lin et al., 2011).

131 **2.2. Landslide inventory**

132 The Forestry Bureau of Taiwan has produced a yearly landslide inventory for the
133 whole Taiwan from 2004 to 2018 (Lin et al., 2013; Chen et al., 2019b), based on visual
134 interpretation of Formosat-2 satellite images (2 m spatial resolution) collected between
135 January and July for each year, and validated with aerial images (25 cm spatial
136 resolution; Lin et al., 2013). These annual landslide maps do not distinguish new
137 landslides that occurred in a specific year from those that were already present.
138 Therefore, to isolate the contribution of new occurrences and/or reactivated failures, we
139 calculated the difference of two subsequent yearly inventories to derive landslide
140 expansion areas for each year under consideration. This preprocessing procedure for
141 landslide maps is the same as our previous study, and further details are provided in
142 Fang et al. (2022). As a result, we obtained 14 yearly landslide inventory maps (**Fig. 1**),
143 with new or reactivated landslides between August 1st of the considered year to July
144 31st of the subsequent one.



145

146 **Fig. 1** (a) Location of the study area; (b) elevation distribution of Taiwan island; (c) a sub-region
 147 showing the slope units partition, and (d, f) spatial distribution of landslides in two sub-regions from
 148 2004 to 2018. Landslides in each time period denotes the expansion area from August 1st of the current
 149 year to July 31st of the next year. This figure is modified from Fang et al. (2022).

150 2.3. Explanatory factors

151 In the context of a space-time modelling implemented, some landslide related factors
 152 can be simplified as constant properties, whereas others may exhibit some degrees of
 153 temporal variation on a daily, seasonally or yearly basis. For this reason, we prepared a
 154 set of static and dynamic factors to build our space-time model. Specifically, we derived
 155 eight static terrain attributes from SRTM DEM data, five of which have already been
 156 employed in Fang et al. (2022): slope, plan curvature, profile curvature, northness, and

157 eastness. In the present study we also obtained three relief-related factors (intensity,
158 range, and variance) to represent the gravitational potential energy across the terrain
159 (Stepinski and Jasiewicz, 2011). Notably, the hillslope relief has appeared in a number
160 of studies dedicated to landslide size (Medwedeff et al., 2020), and has proven to be a
161 dominant covariate in landslide size predictive modelling (Lombardo et al., 2021). We
162 also considered the variation in lithological conditions, expressed through 15 classes
163 derived from a 1:250,000 scale geological map (see Appendix A for the descriptions).
164 We also generated the Euclidean distance to faults, derived from a 1: 50,000 scale fault
165 map. The above two geological factors can be accessed via the Central Geological
166 Survey of Taiwan (<https://www.geologycloud.tw/>). Furthermore, we used slope units
167 derived from the DEM as our basic terrain unit. We considered the dual interaction
168 between longitude and latitude of each mapping unit centroid to represent the spatial
169 structure of the Taiwan landscape. All the above factors belong to the stationary set of
170 predictors we selected for our space-time modelling procedure.

171 As for the dynamic ones, we opted to include rainfall, normalized difference
172 vegetation index (NDVI), and a yearly function of the timesteps between subsequent
173 inventories. Our previous study showed that maximum daily rainfall is an appropriate
174 dynamic factor in a yearly space-time landslide susceptibility model for Taiwan (Fang
175 et al., 2022). Therefore, we collected the rainfall estimates from 188 meteorological
176 stations and interpolated the yearly daily maximum rainfall via a cokriging routine,
177 which used elevation as a parameter to represent the orographic effect on the
178 precipitation patterns. To describe the effect of vegetation, we calculated the yearly
179 maximum NDVI based on Landsat-7 images via the Google Earth Engine platform.
180 Ultimately, the temporal effect on landslide sizes was brought into the model as a
181 function of the timesteps between subsequent landslide occurrences, that is, we labeled

182 each slope unit with an ID to indicate which yearly landslide inventor it belongs to .

183 **3. Methodology**

184 **3.1. Mapping and temporal units**

185 Determining appropriate mapping and temporal units is important for any space-time
186 modelling. To geographically partition the landscape, we generated slope units (SUs)
187 as our reference terrain units for they well reflect the slope morphodynamics (Guzzetti
188 et al., 1999), and they cover the landscape units between sub-catchment divides and
189 streams, making them particularly suitable for landslide modeling (Carrara, 1988).
190 Since our study focuses on the whole main island of Taiwan which has extensive flat
191 areas along the coasts, we used the r.geomorphon module (Jasiewicz and Stepinski,
192 2013) available in GRASS GIS to outline flat areas. In a subsequent step, we excluded
193 them from the analysis performed by the r.slopeunits software (Alvioli et al., 2016), a
194 tool to automatically delineate SUs on the basis of an aspect-homogeneity criterion.
195 This resulted in 46,074 polygons with a mean SU area of 589,844 m² and a standard
196 deviation of 395,973 m². As for the temporal dimension, we chose a temporal unit of
197 one year (from August 1st of the current year to July 31st of the next year). The resulting
198 space-time domain therefore featured 645,036 units, made of 46,074 SUs and repeated
199 over the 14 temporal units. Further details on these aspects can be found in Fang et al.
200 (2022).

201 Each of these units need to be assigned with a covariate value, for the covariates
202 listed in Section 2.3 (see **Table 1**). The spatial extent of the SUs requires an upscaling
203 step. In fact, a large number of grid-cells can be hosted in a SU, from which a
204 distribution of potential values can be derived. Thus, to account for the associated intra-
205 SU variability, we derived two statistical moments in the form of the mean and standard
206 deviation for all terrain attributes, distance to faults, and NDVI. As for the lithological

207 characterization of each SU, we extracted the class with the largest areal extent as
208 representative for the whole SU. Because the maximum daily rainfall has a more even
209 distribution over the SUs, we only extracted the mean precipitation value per SU, and
210 not the standard deviation.

211 Unlike landslide susceptibility modelling where the focus is given to landslide
212 presence/absence data, our size model requires an information on the planimetric
213 landslide extent per SU. To estimate this extent and later use it as the response variable
214 of our model, we computed the sum of all landslide areas falling within each SU and
215 converting the resulting heavy-tailed distribution by using the logarithmic
216 transformation. From this, we extracted the positive part of the landslide area
217 distribution (removing the zeros or those units with no landslides) giving rise to a
218 spatio-temporal domain made of 119,545 SUs (with a total landslide area of 1732.55
219 km²).

220

221

222

223

224

225

226

227

228

229

230

231

Table 1 Summary of covariates used in the study.

Type	Covariates	Description
Static	Mean slope	Mean and standard deviation (SD) of morphological factors in each slope unit
	Slope-SD	
	Mean plan curvature	
	PlanCurv-SD	
	Mean profile curvature	
	ProfileCurv-SD	
	Mean northness	
	North-SD	
	Mean eastness	
	East-SD	
	Mean relief intensity	
	ReliefInt-SD	
	Mean relief range	
	ReliefRan-SD	
Mean relief variance		
ReliefVar-SD		
Dynamic	Mean distance to faults	Mean of distance to faults in each slope unit
	FaultDis-SD	SD of distance to faults in each slope unit
	Lithology	Majority class in each slope unit.
	Slope unit area	Area of each slope unit
	Spatial location	longitude and latitude of the centroid in each SU
	Maximum daily rainfall	Mean of rainfall per year in each slope unit
	Mean NDVI	Mean of NDVI per year in each slope unit
NDVI-SD	SD of NDVI per year in each slope unit	
	Time period	Time period ID for each slope unit

233

234 **3.2. Generalized additive model**

235 A generalized additive model (GAM) can estimate linear and nonlinear effects
236 between explanatory and target variables (Goetz et al., 2011). As a result, these models
237 can provide satisfying performance while maintaining flexibility and interpretability.
238 GAMs have been successfully used in a number of spatially-explicit models for
239 landslide occurrences, dedicated to landslide susceptibility (e.g., Steger et al., 2016;
240 Titti et al., 2021) and intensity assessments (e.g., Lombardo et al., 2019). The same
241 GAM framework has recently been used by Lombardo et al. (2021) through assuming
242 that landslide planimetric area in a terrain unit follows a log-Gaussian distribution,
243 which is the same assumption we will make in this manuscript. The difference resides
244 in our extension of the same framework to the space-time domain. To do so, we fitted
245 a space-time Log-Gaussian GAM by using the ‘mgcv’ R-package (Wood, 2011).

246 Notably, our GAM formulation can be denoted as follows:

$$\begin{aligned} \log(A_L) &\sim \mathcal{N}(\mu, \sigma^2), \\ g(\mu) &= \alpha + \sum_{i=1}^m S_i(x_i) + \sum_{j=1}^n \beta_j^{litho} x_j + S(lon, lat) + S(time) \end{aligned} \quad (1)$$

247 where A_L is the cumulative landslide planimetric area in each slope unit, μ and σ^2 are
248 the mean and variance for Gaussian distribution respectively, g is the log link, α is the
249 global intercept, S_i are the smooth function associated with a number of nonlinear
250 covariates x_i (all covariates except lithology and spatial effect), β_j^{litho} is the regression
251 coefficient for the lithology class x_j , $S(lon, lat)$ denotes the interaction smooth of
252 longitude and latitude to account for the spatial structure. $S(time)$ represents the
253 smooth function associated with temporal effect between subsequent landslide
254 occurrences.

255 On a final note, the 119,545 Sus analyzed here do not represent the whole space-time
256 domain expressed across the 14 examined years and the whole landscape of Taiwan.
257 They are rather a subset of it corresponding to the positive part of the landslide size
258 distribution. Because of this, we stress here that our modeling protocol will make us of
259 the fitted model to extent the prediction over the remaining 525,491 SUs. We are aware
260 that these SUs did not undergo any landsliding but we opted to graphically simulated
261 over those units to get a full picture, albeit overestimated, of the expected landslide size
262 distribution over the whole space-time domain.

263 **3.3. Model evaluation**

264 Below we describe the metrics and schemes to evaluate the model performance both
265 in terms of goodness-of-fit and predictive performance. In both cases, three numerical
266 metrics are considered namely, mean absolute error (MAE), root mean square error

267 (RMSE), and Person correlation coefficient (R). We recall here that we only use
268 119,545 SUs with mapped landslides for landslide size modelling. For the goodness-
269 of-fit, we fitted an explanatory model with 100% of the dataset and interpreted the
270 effects of covariates. Aside from above numerical metrics, we used three common
271 graphical methods to assess the goodness-of-fit (Wood, 2006), namely, plot of observed
272 versus fitted values, QQ plot, and histogram of residuals.

273 For the predictive performance, we used the above three numerical metrics and the
274 plot of observed versus predicted values to evaluate the predictive performance.
275 Moreover, four different cross-validation schemes were implemented for validation,
276 namely, random 10-fold cross-validation (10fold-CV), spatial leave-one-out cross-
277 validation (S-CV), temporal leave-one-out cross-validation (T-CV), and spatio-
278 temporal leave-one-out cross-validation (ST-CV). Note that the four cross-validation
279 procedures have been successfully used to model space-time landslide susceptibility in
280 the same study area (Fang et al., 2022). We thus briefly introduced these validation
281 procedures here. The 10fold-CV is the most common and conservative scheme to assess
282 model performance. It randomly splits the original dataset into 10 equal-sized subsets
283 and repeatedly fits the model with nine subsets and validates with the one left-out. The
284 S-CV scheme first divides the whole dataset into 12 spatial subsets by considering the
285 administrative partitioning of Taiwan, and then repeatedly leaves out one of the twelve
286 subsets for validation and fits the model with the remaining subsets. Similar to S-CV,
287 the T-CV is based on 14 temporal subsets and validated year by year. As for the ST-
288 CV, it generates 168 subsets based on above 12 spatial partitioning and 14 time intervals,
289 and then executes the leave-one-out validation procedure.

4. Results

4.1. Model construction and goodness-of-fit

In the modelling process, we first implemented a forward-stepwise procedure to assess whether a given covariate would provide effective information for landslide size modelling. This covariate selection procedure relied on the Akaike information criterion (AIC; Akaike, 1974), where a lower AIC value is diagnostic of a better model. Specifically, we first ran all single-covariate models, from which we selected the covariate with the lowest AIC value. Then, we focused on selecting the best two-covariate model, then three-covariate one and so on, each time choosing the combination that has led to the minimum AIC. This process was then stopped when the decrease in AIC value fell below a threshold of 100. **Table 2** shows the overview of the forward-stepwise procedure described above. The final covariate set includes slope unit area, NDVI-SD, maximum daily rainfall, Mean NDVI, time periods, coordinate of slope units, mean profile curvature, mean slope, Slope-SD, mean eastness, lithology, ReliefVar-SD, and mean plan curvature.

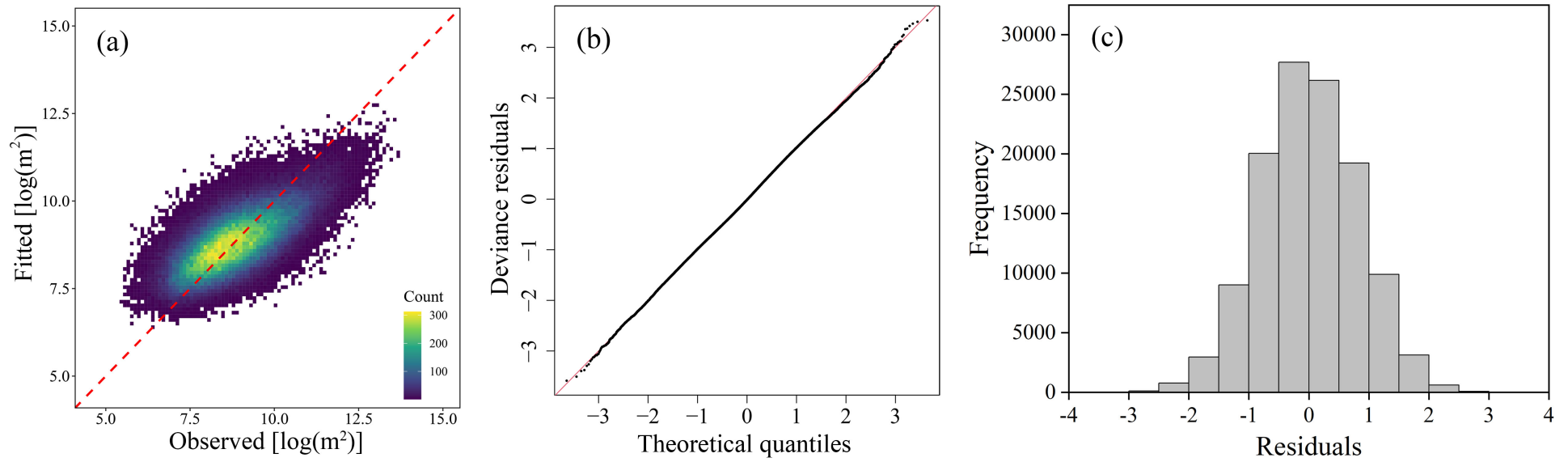
Table 2 results of the forward-stepwise covariate selection

Step	Selected covariate	AIC	Improvement
1	Slope unit area	346734	/
2	NDVI-SD	317164	29570
3	Maximum daily rainfall	308237	8927
4	Mean NDVI	302228	6009
5	Time periods	297896	4332
6	Coordinate of slope units	296051	1845
7	Mean profile curvature	294976	1075
8	Mean slope	293829	1147
9	Slope-SD	293121	708
10	Mean eastness	292443	678
11	Lithology	292141	302
12	ReliefVar-SD	291894	247
13	Mean plan curvature	291722	172
14	Mean northness	291657	65

This covariate set was used as the base to construct an explanatory space-time model.

Fig. 2 shows an overview of the goodness-of-fit via three criteria, namely, observed

308 versus fitted values, QQ plot, and histogram of residuals (all in log-scale). Inspection
309 of **Fig. 2 (a)** shows that the model achieves a high degree of agreement between the
310 observed and fitted landslide areas per slope unit. The QQ plot presents deviance
311 residuals against theoretical quantiles of the deviance residuals distribution (Wood,
312 2006). In **Fig. 2 (b)** and **(c)**, we observe that the QQ plot is close to a straight line and
313 the histogram of residuals is consistent with normality, indicating an excellent fitting
314 performance. In addition, we also calculated the statistical criteria for fitting evaluation,
315 that is, the MAE, RMSE, and R is 0.657, 0.817, and 0.673, respectively. Overall, our
316 model thus shows a satisfying goodness-of-fit.



317

Fig. 2 Goodness-of-fit of the model: (a) observed versus fitted plot (in log-scale), (b) QQ plot and (c) histogram of residuals.

4.2. Covariates' effect

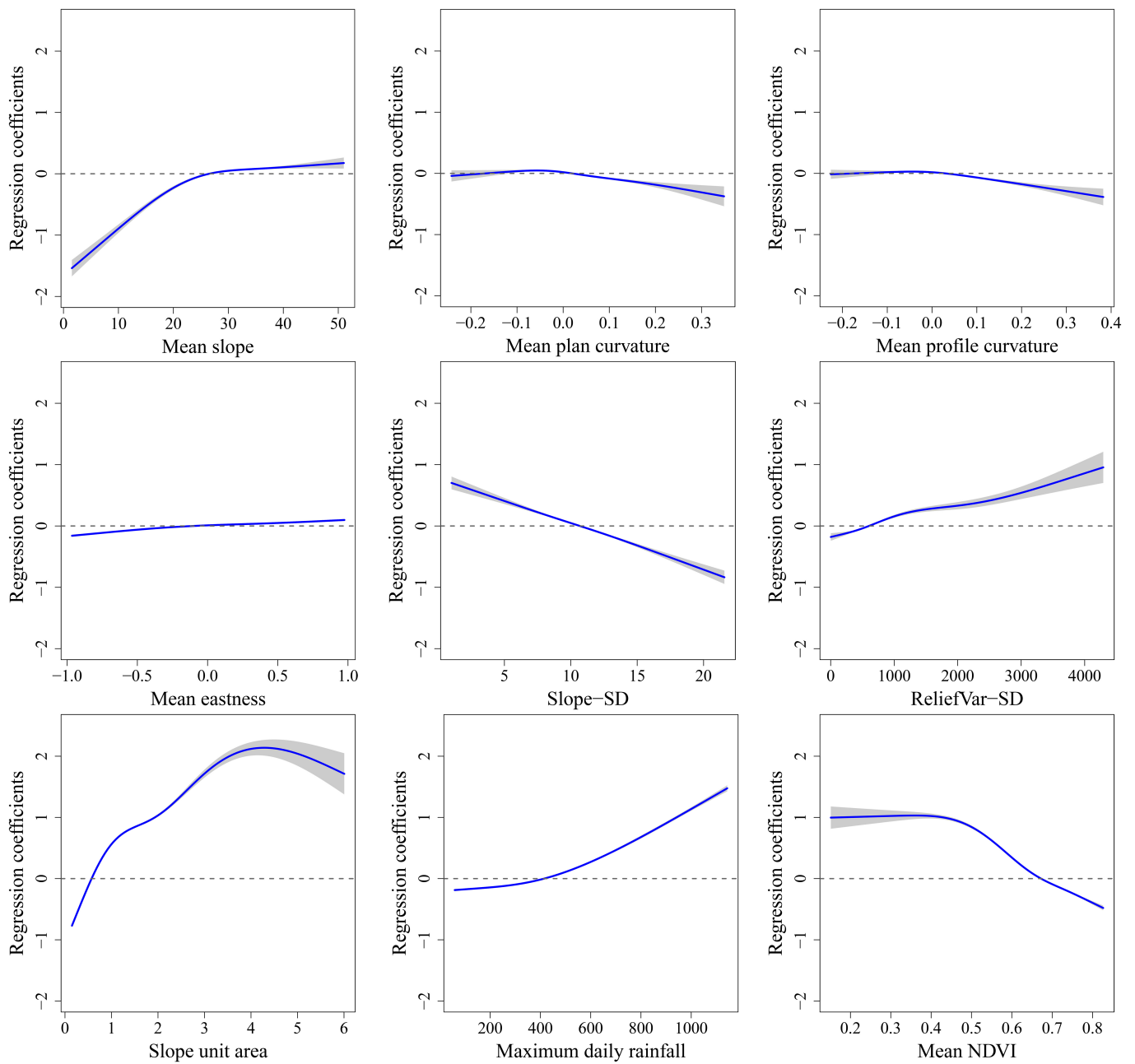
318

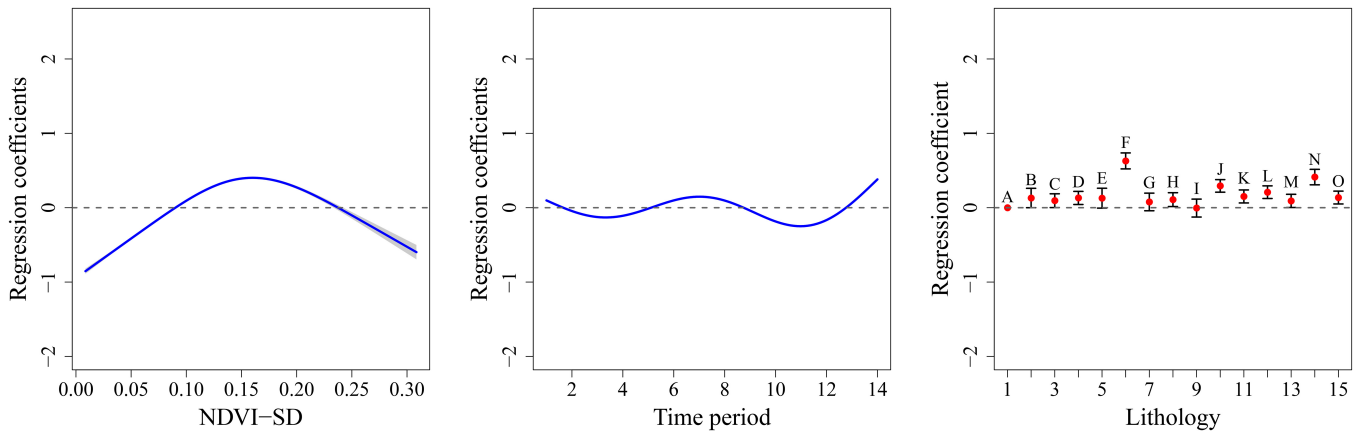
319 The effects of all covariates with estimated 95% confidence intervals are shown in
320 **Fig. 3**. Slope steepness, with a narrow confidence interval, has a positive effect on
321 landslide size above 26° . Plan curvature and profile curvature show similar nonlinear
322 effects on landslide size estimation, and maintain negative effects above 0.02 and 0.03,
323 respectively. The effect of eastness indicates that slope units facing east are expected
324 to have large landslide areas. Although we allowed the regression coefficients of all
325 covariates to vary nonlinearly, the Slope-SD shows a linear effect on landslide size. We
326 considered this as the best way to represent the effect of Slope-SD optimized by the
327 smoothness selection procedure. The ReliefVar-SD has a positive effect on landslide
328 size when the value is above 609. For the SU-Area, it maintains a negative effect on
329 landslide size until the value reaches 5.6 km^2 .

330 Rainfall is a key dynamic factor related to landslide occurrences. In our study, the
331 maximum daily rainfall for each time period was selected for modelling. Inspection of
332 **Fig. 3** shows that the maximum daily rainfall has very narrow confidence intervals and
333 presents a positive effect with rainfall above 420 mm per day. And, the regression
334 coefficient increases with the daily maximum rainfall. For the dynamic factor of NDVI,
335 the mean NDVI maintains a positive effect on landslide size until 0.67, and then the
336 regression coefficient decreases with the NDVI value. The NDVI-SD has a significant
337 and positive effect on landslide size from 0.09 to 0.23. For the lithology covariate, 11
338 classes show significant and positive effects on landslide area estimation. Specifically,
339 the class F (Mudstone intercalated with allochthonous material) has the highest positive
340 effect, followed by the class N (Shale, siltstone, and sandstone) and class J (Sandstone,
341 mudstone, and shale).

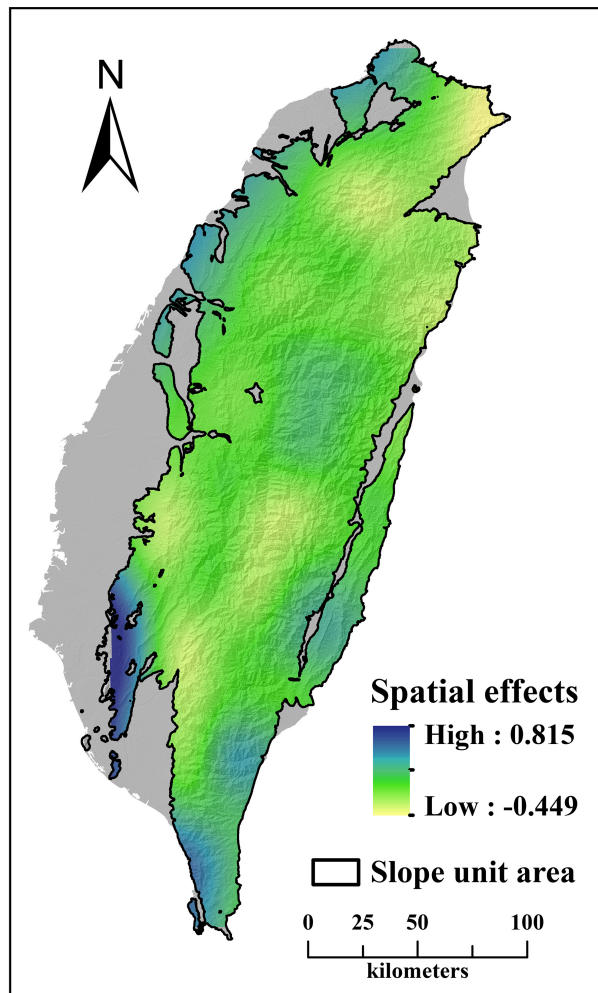
342 We recall here that we considered the temporal and spatial effects in the landslide

343 size modelling through a function of time and a function that expresses the interaction
 344 of latitude and longitude, respectively. In **Fig. 3**, we observe that the temporal function
 345 shows a marked oscillation, with a “wavelength” of about 8 years. For the spatial effect
 346 (**Fig. 4**), some clusters emerged in certain regions. For example, the central and
 347 northeast parts show negative effects on landslide size, whereas the southwest and
 348 northwest fringe parts present positive effects.





349 **Fig. 3.** Summary of effects of covariates. For lithology, the red dots show the regression
 350 coefficient, and the vertical segments are the 95% confidence intervals. For other nonlinear
 351 effects, the blue curves show the regression coefficient and the shadowed polygons denotes the
 352 95% confidence intervals.
 353



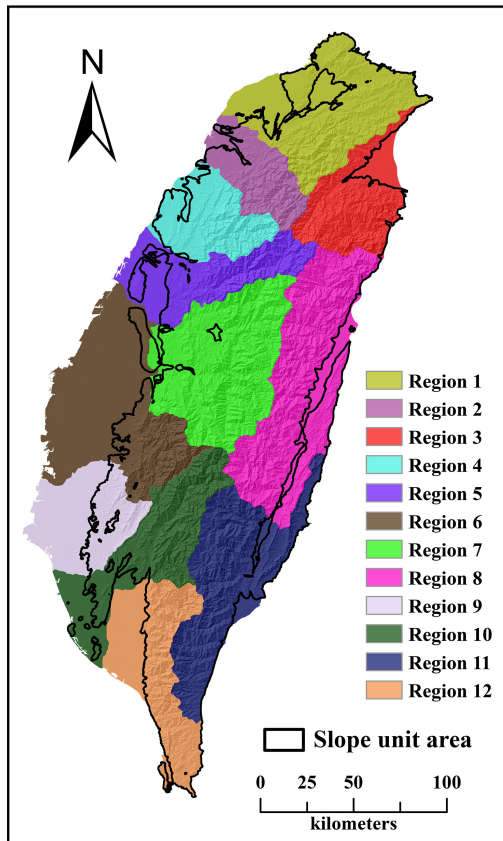
354
 355 **Fig. 4.** Spatial effect in the space-time model

356 4.3. Space-time predictive performance

357 Aside from the goodness-of-fit assessment, it is also important to test whether the

358 model predicts well “unknown” samples distributed both in space and time. Thus, we
359 performed a suite of CV procedures to assess the predictive performance of the
360 proposed model in different perspectives, namely, 10fold-CV, S-CV, T-CV, and ST-
361 CV. Note that the space division for S-CV and ST-CV is based on the administrative
362 unit of Taiwan, as shown in **Fig. 5**, and the description of different sub-regions is given
363 to Appendix B. To maintain a comparable number of samples in each sub-region, we
364 merged some small counties or cities.

365 The predictive performance of 10fold-CV, S-CV, and T-CV is presented in **Fig. 6**,
366 measured via MAE, RMSE, and Pearson correlation coefficient (R). We observe that
367 the 10fold-CV achieves the most stable results among the three CV schemes and its
368 three evaluation indices do not vary significantly. This is because the 10fold-CV
369 randomly selects validation samples from the whole space-time domain, thus limiting
370 the spatial and temporal perturbation induced with respect to the original data
371 distribution. Thus, we extended our validation scheme to incorporate S-CV and T-CV
372 procedures. In **Fig. 6**, the T-CV shows larger metric fluctuations compared to S-CV,
373 indicating that the temporal perturbation to the data distribution is more prominent than
374 the spatial one, although our space-time model still returns good performance. To
375 further investigate the predictive ability of our model across different time periods or
376 geographical regions, we summarize the relative variations in performance in **Fig. 7**.
377 There, we observe that the MAE and RMSE show similar fluctuations in the two CV
378 procedures. This may be because both indices represent the error between the observed
379 and predicted landslide areas. As for the R index, the S-CV returns the highest value
380 while predicting over the sub-region 5, and achieves relatively low values of less than
381 0.6 while predicting over sub-region 1 and 2. For the T-CV procedure, the model has
382 the highest R value in T6, and the lowest in T5.



383

384

Fig. 5. Spatial sub-regions for validation.

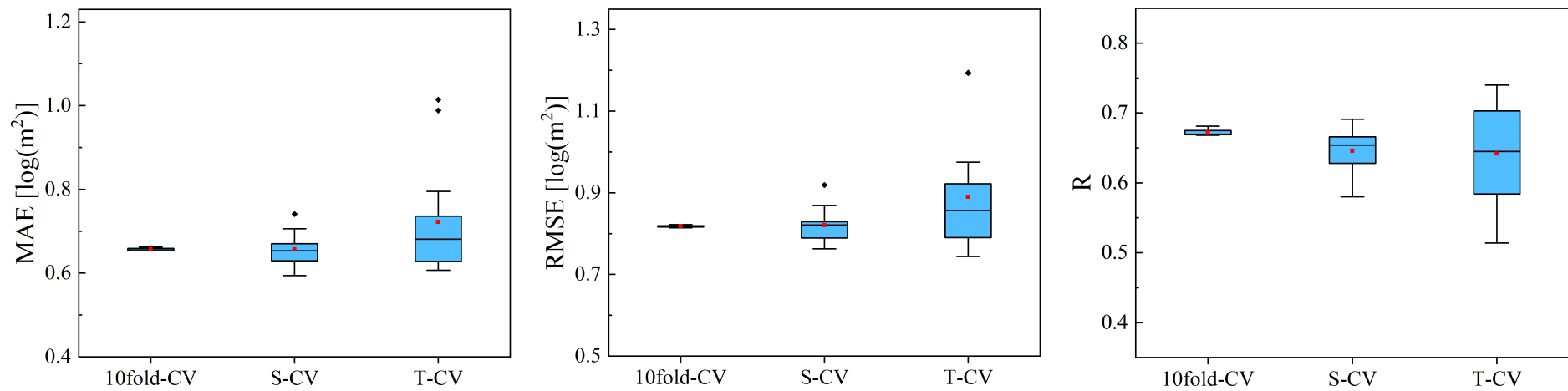


Fig. 6. Predictive performance of 10fold-CV, S-CV, and T-CV

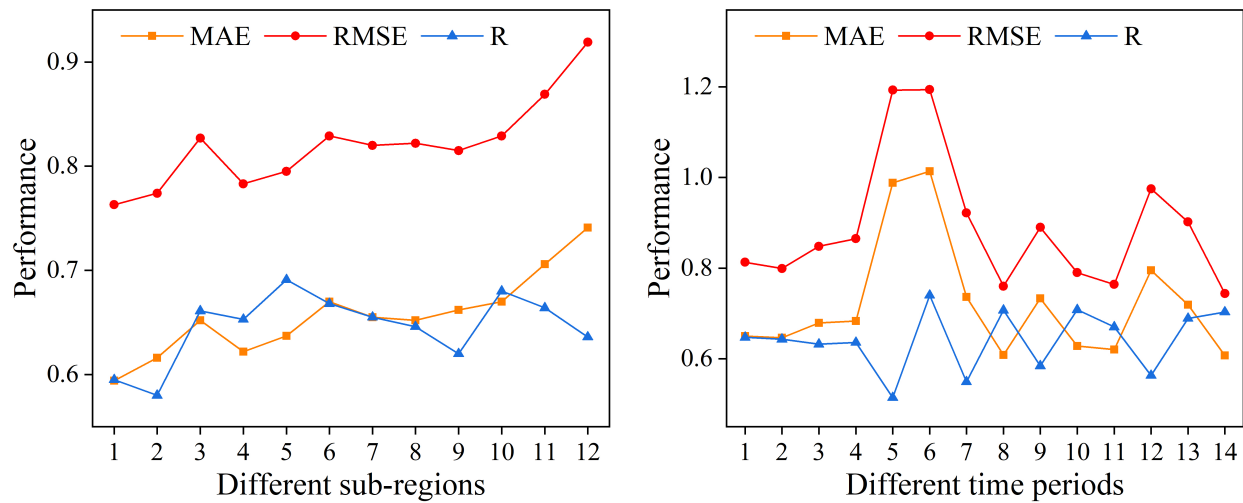


Fig. 7. Performance variations of different sub-regions and time periods.

388 Finally, we implemented a ST-CV procedure to contextually assess the size
389 predictive performance in both spatial and temporal dimensions. We recall here that we
390 divided the whole space-time domain into 168 parts with 12 spatial and 14 time
391 intervals, and samples in each part were validated separately. **Fig. 8** shows the
392 predictive performance of the ST-CV scheme. Note that each boxplot denotes the
393 temporal variation in a given spatial sub-region. We observe that the model achieves a
394 good prediction performance with mean MAE, RMSE, and R values of 0.661, 0.817,
395 and 0.646, respectively. Inspection of the boxplots shows that three evaluation indexes
396 have greater fluctuations in northern (sub-region 1 and 2) and southern (sub-region 11
397 and 12) parts of Taiwan than other sub-regions. Moreover, we can observe that the ST-
398 CV scheme results in higher performance variations than 10-fold CV, S-CV, and T-CV,
399 because this validation procedure exaggerates both spatial and temporal difference.

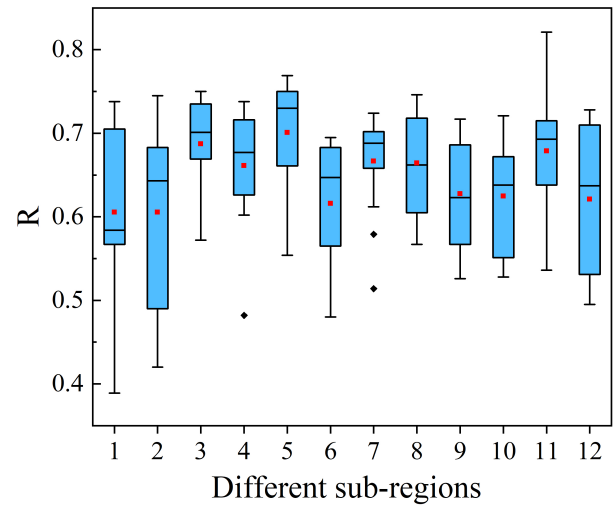
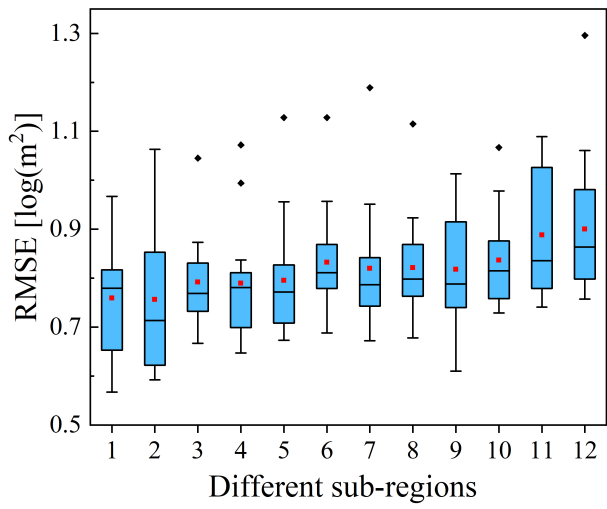
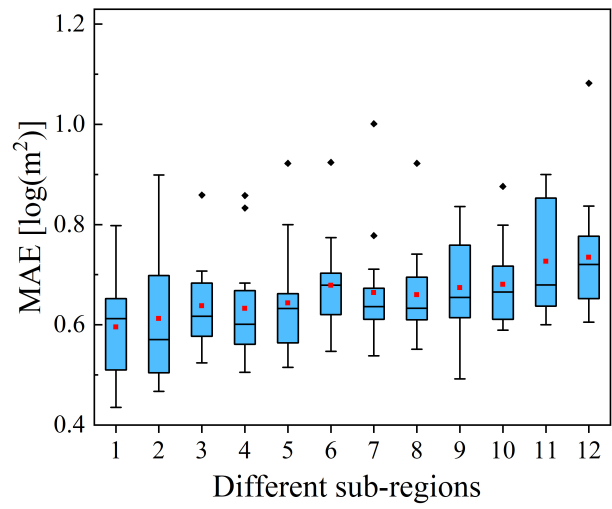
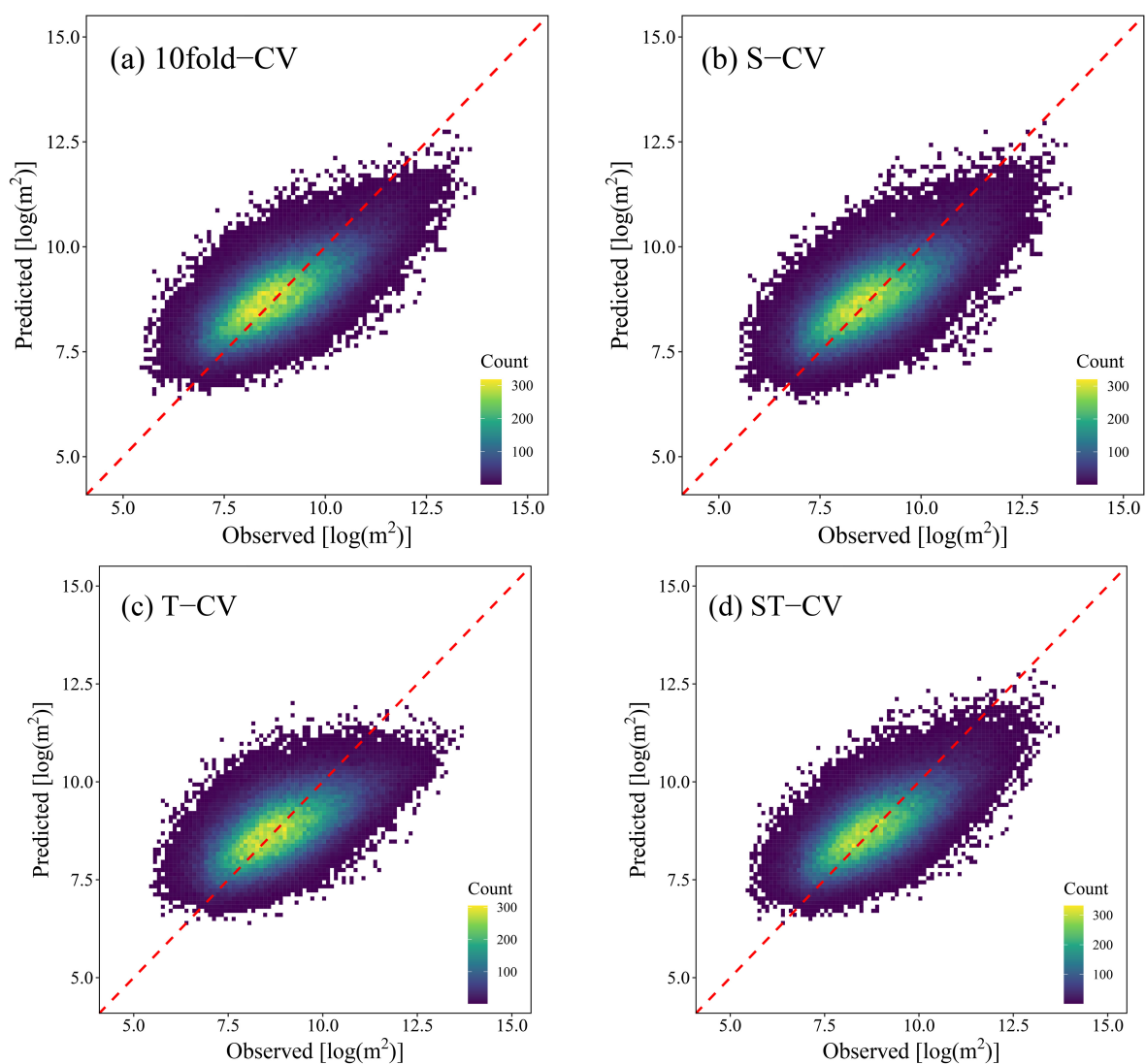


Fig. 8. Predictive performance of ST-CV

400

401 We also provide the scatter plots to show the visual agreement between observed and
 402 predicted landslide areas for different CV schemes (**Fig. 10**). One can see how much
 403 the predicted values agrees with the actual ones, for they roughly aligned with the 45°
 404 line. Inspection of **Fig. 10** shows that all models achieve reasonable predictive
 405 performance, and the 10fold-CV, S-CV, and ST-CV presents slightly better aligned
 406 spread along the 45° line than T-CV. Moreover, four models exhibit slightly
 407 overestimations in the left tail and underestimations in the right tail.

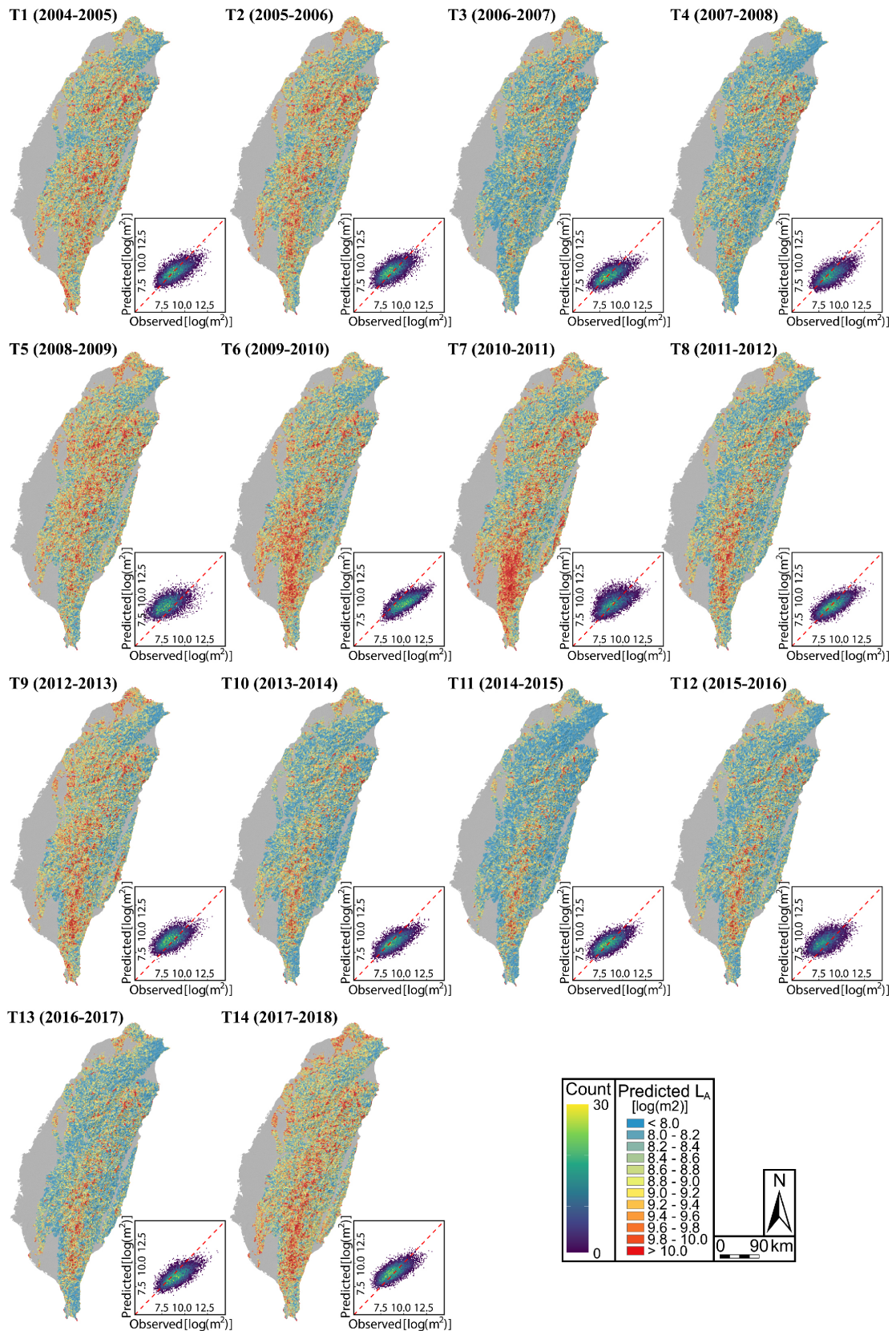


408 **Fig. 9.** Observed versus fitted plots (in log-scale) for different CV schemes.

409 **4.4. Landslide size mapping**

410 We used the T-CV procedure to predict the landslide size maps of the 14 time periods,

411 as shown in **Fig. 10**. We also present the plot of predicted versus observed areas for
412 each landslide size predictive map. We can observe that the 14 landslide size maps have
413 strong spatial variations over time. A cluster of larger landslide areas in southern
414 Taiwan can be seen, appearing in T6 (2009-2010), peaking at T7 (2010-2011), then
415 gradually disappearing. Inspection of these scatter plots shows that the model obviously
416 overestimates the landslide size in T5 (2008-2009), T9 (2012-2013), and T12 (2015-
417 2016), and underestimates the landslide size in T6 (2009-2010), T10 (2013-2014), and
418 T13 (2016-2017). Although the model predicts well and produces values aligned with
419 the along the 45° line in other years, a slightly overestimation in the left tails, and
420 underestimation in the right tails can be observed.



421

422 **Fig. 10.** Landslide size predictive maps in Taiwan from 2004 to 2018. Scatter plots shows the
 423 predictive versus observed landslide areas for each time period.

5. Discussion

5.1. Model performance

Our space-time-size model goes beyond the traditional susceptibility model to estimate the landslide planimetric areas across within SUs, and extend the spatially-explicit size model (Lombardo et al., 2021) into both spatial and temporal dimensions. Our explanatory model achieves a satisfying goodness-of-fit (**Fig. 2**) and is able to portray the effects of covariates in an interpretable manner (**Fig. 3**). Moreover, measuring the predictive performance of the size model is also important. Lombardo et al. (2021) implemented a general spatial validation, and Moreno et al. (2022) then extended it into a spatially explicit validation to evaluate the spatial transferability of the model across specific regions. However, as our model is contextually constructed over space and time, we need to explore the prediction ability across the whole space-time domain. We presented a full suite of cross-validation routines from the spatial, temporal, and spatio-temporal standpoints (see Section 3.3). Overall, the predictive performance estimated via different validation schemes achieves good results confirmed through numerical metrics (**Fig. 6** and **Fig. 8**) and graphical methods (**Fig. 9**). We stress here that another improvement in cross-validation process is the implementation of ST-CV. This can be viewed a complete spatio-temporal validation scheme capable of exploring the prediction ability of landslide size models over any time period and any geographic location.

However, there are still some limitations or some aspects can be further improved in this work. First, the landslide area is expressed on a logarithmic scale and is then assumed to follow a Gaussian distribution. Note that this logarithmic transformation is common used in landslide magnitude studies (Guzzetti et al., 2002; Malamud et al., 2004; Medwedeff et al., 2020). Although the logarithm function is monotonous

449 increasing, the landslide area on such scale is hard to interpret for practical usage. On
450 the other hand, converting the prediction results from logarithmic scale into actual
451 expression (m^2) would exacerbate the difference in very low or very large areas
452 (Lombardo et al., 2021). This is likely the result of the Gaussian likelihood choice,
453 which struggles to predict well the behavior in the tail of a skewed distribution. This
454 also stands out in our model results, where we can always observe a slight
455 overestimation in the left tail and a slight underestimation in the right tail. This is valid
456 not only in the predictions of all space-time domain (**Fig. 9**), but also when we look at
457 specific temporal predictions (**Fig. 10**). We thus envision future efforts to test a more
458 suitable probability distribution for space-time landslide size modelling. Second, the
459 space-time domain in our size model is constrained by present and past situations. It
460 lacks actual prediction for specific future time period. We envision this to be improved
461 by simulating future scenarios of dynamic factors, following a simulation approach
462 analogous to the scheme proposed by Lombardo and Tanyas (2021), in the context of
463 earthquake scenarios for landslide susceptibility.

464 **5.2. Interpretation of covariates**

465 A good model should not only maintain high performance, but also need to be
466 interpretable. Here, we discuss the effects of covariates on space-time size modelling
467 from a geomorphological or statistical perspective (see **Fig. 3**). The terrain slope shows
468 a monotone trend with the regression coefficient, indicating that steeper landscapes are
469 expected to generate larger mass movements. This observation is line with Katz et al.
470 (2014) who performed numerical simulations to study the controls on landslide size.
471 The authors concluded that the detachment of material from steeper slopes largely
472 disintegrates while propagating downhill, thus covering a larger planimetric area upon
473 arrest. The plan curvature and profile curvature negligibly contribute to explaining the

474 landslide size approximately up to 0, and the two covariates show negative effects on
475 landslide size from the threshold onward. It may be because landslide materials are
476 difficult to converge into the sidewardly convex terrain, and the erosion may not prevail
477 in upwardly concave terrain (Ohlmacher, 2007). Furthermore, some studies find that
478 east-facing slopes in Taiwan region have a high correlation with landslide occurrences
479 (Lee, 2013; Chen et al., 2019a; Fang et al., 2022), we extended this relationship into
480 landslide size in this study. As for Slope-SD, this can be considered a proxy to represent
481 the topographical roughness across a give SU. It shows a completely linear effect with
482 landslide size and its effect decreases as the SD value increase. This may be because
483 the SU with a low standard deviation of slope has a smooth and homogeneous landscape,
484 and a large amount of materials will mobilize once the landslide occurs. Or an
485 alternative explanation may have to do with rock mass strength. In fact, strong materials
486 tend to produce rougher landscapes, i.e., large steepness variations. Conversely, softer
487 or unconsolidated material can loosely drape over the bedrock, giving raise to large
488 failures. In this work, we also selected the relief variance (ReliefVar-SD) to describe
489 the variability of elevation information in a circle, because a higher locations
490 intrinsically have a larger gravitational potential energy to be converted into landslide
491 kinematics and thus into overall planimetric extent (Lombardo et al., 2021). This initial
492 hypothesis is confirmed in the ReliefVar-SD plot, where this parameter positively
493 contributes to the increase of landslide sizes. The slope unit area shows a negative effect
494 on very small SUs, while the contribution appears to positive on larger SUs, which is
495 associated with previous study (Bryce et al., 2022). For lithology, the class F (Mudstone
496 intercalated with allochthonous material) has the highest positive effect on landslide
497 size. The Class F often coincides with badland landscapes in Taiwan, which are prone
498 to landsliding, debris flows, and fluvial erosion (Yang et al., 2021). The class N (Shale,

499 siltstone, and sandstone) and class J (Sandstone, mudstone, and shale) also show
500 positive effects on landslide size, which is agreement with the observations made by
501 Wu and Chen (2009), as the sandstone, shale and mudstone have been attributed by the
502 authors with the highest landslide rates in central Taiwan.

503 Upon completing this overview of the contribution of static covariates, below we will
504 summarize how the dynamic ones entered the landslide size estimation. Fang et al.
505 (2022) discussed how to appropriately use rainfall-related covariates for landslide
506 space-time susceptibility modelling in Taiwan, and concluded that the maximum daily
507 rainfall is the most suitable by considering the landslide background, available rainfall
508 data, and the involved spatio-temporal scale. In our study, we also used the maximum
509 daily rainfall to express the climatic control over landslide sizes. We observe that the
510 regression coefficient increases with the rainfall, with the maximum daily rainfall
511 contribution becoming positive for values greater than 420 mm per day. This monotone
512 increasing trend is surprisingly similar to the one shown in our space-time susceptibility
513 model (Fang et al., 2022), although the rainfall threshold appears lower than the one
514 retrieved for the susceptibility case (740 mm per day). Further studies in lines with the
515 considerations above could open up discussion on rainfall thresholds models useful
516 beyond the pure landslide occurrence case (Segoni et al., 2018; Monsieurs et al., 2019;
517 Wang et al., 2021) and towards the size one instead.

518 NDVI was also used dynamically in time to reflect the effect of the surface vegetation
519 condition. In **Fig. 3**, NDVI clearly maintains a positive effects on landslide size for low
520 values and transitions to a negative regression coefficient for values above 0.67. This
521 is reasonable because high vegetation cover could increase shallow soil shear strength
522 and reduce erosion (Schwarz et al., 2010). As for the NDVI-SD, its contribution appears
523 to be negative for low variation of NDVI within a SU. This effect transitions to positive

524 for medium variations of the NDVI and goes back to negative for large variations within
525 a SU. This is a complex behavior to interpret, but one explanation could be that a low
526 NDVI-SD value indicates that the vegetation coverage in the SU is uniform, and this
527 situation is likely to occur in SUs that are almost fully covered by vegetation or bare
528 land. Conversely, a SU with high NDVI-SD value may denote a complex and
529 heterogeneous landscape environment, whose contribution to the landslide size may be
530 less straightforward to explain.

531 Aside from above environmental covariates, our model also considered the temporal
532 and spatial relationship between SUs with different landslide areas. Specifically, we
533 introduced an additional covariate, i.e., each SU was assigned a time period ID. We
534 find that the temporal covariate shows significant oscillations. The two adjacent highest
535 positive effects or lowest negative effects are separated approximately 8 years apart.
536 This could indicate a return period for landslide size variation in time, or being
537 diagnostic of a larger periodic effect due to harsher climatic conditions to which Taiwan
538 may have been exposed in the past. As for the spatial effect, we considered the
539 interaction between longitude and latitude to account for the spatial structure between
540 SUs. In other words, this effect constrains close SU to behave more similarly as
541 compared to SU that are far apart, in relation to the expected landslide size. In turn this
542 can lead to clusters of landslide size, which the spatial effect denoted in specific regions
543 of Taiwan.

544 **5.3. Hazard considerations**

545 The landslide hazard definition initially from Varnes (1984), and then improved by
546 (Guzzetti et al., 2005), divides the probability assessment into three components of
547 spatial probability (susceptibility), temporal probability, and size probability. Landslide
548 susceptibility has been successfully estimated based on different methods (Reichenbach

549 et al., 2018; Merghadi et al., 2020). In recent years, two components of spatial and
550 temporal aspects are simultaneously modelled in landslide prediction studies. For
551 example, Lombardo et al. (2020) is the first to build a Bayesian version of Poisson
552 space-time GAM for landslide occurrences. They went beyond traditional susceptibility
553 models to perform space-time estimation of the landslide counts. Wang et al. (2022)
554 tested a space-time binomial generalized linear model for hydro-morphological process
555 susceptibility across China. And, we recently implemented a Bayesian version of a
556 binomial GAM to estimate the space-time susceptibility in Taiwan (Fang et al., 2022).
557 However, the above space-time models neglect the landslide size, which is otherwise
558 accounted for in this work. As a result, by estimating the planimetric area of mass
559 movements per SUs in time we fulfill two components of the hazard definition. We
560 therefore consider this improvement a step towards a next generation model where
561 different aspects of the hazard definition will be estimated jointly.

562 **6. Conclusions**

563 We implemented a space-time size model in the main island of Taiwan from 2004 to
564 2018. The model corresponding to a Log-Gaussian GAM is capable to estimate
565 landslide planimetric areas per slope unit across the whole space-time domain. We
566 validated the predictive performance of the model based on a complete suite of cross-
567 validation routines by considering the spatial, temporal, and spatio-temporal
568 perspectives. The results indicate that the space-time characteristics of landslide size
569 can be captured from stationary and dynamic factors, as well as the relationships
570 between slope units that are close in space and time. This is a significant improvement
571 that goes beyond the traditional susceptibility modelling to perform space-time
572 estimation of landslide size. Moreover, this model is also an extension of space-time
573 susceptibility model, which provide a promising step towards an operational use of

574 landslide size estimation. However, our model does not fully satisfy the definition of
575 hazard as it lacks the information on whether a slope is actually stable or unstable. For
576 this reason, we envision our future efforts to be dedicated to a combinatory model where
577 all requirements of the landslide hazard definition will be addressed in a single
578 analytical protocol. If so, this could further provide the basis for an operational space-
579 time risk model, where the expected loss due to landslides can be probabilistically
580 simulated before reaching the emergency phase. Before reaching this stage though,
581 another potential improvement to be explored could be finding a more suitable
582 probability distribution to reduce the misestimates in the tails. Or even better, by
583 directly modelling the landslide size in square meters instead of using a logarithmic
584 transformation. Overall, we expect our space-time size prediction model to place a new
585 brick in the landslide literature upon which laying the foundation for future advances
586 in data-driven applications. This new data-driven prototype better portrays the overall
587 landslide information across a given the landscape, and in the hope of triggering similar
588 experiments within the geoscientific community.

589 **Acknowledgement**

590 This work was supported by the Joint Funds of the National Natural Science Foundation
591 of China (U21A2013), the National Natural Science Foundation of China (61271408),
592 the China Scholarship Council (No. 202106410043), and the Fundamental Research
593 Funds for National Universities, China University of Geosciences (Wuhan). This article
594 was also partially supported by King Abdullah University of Science and Technology
595 (KAUST) in Thuwal, Saudi Arabia, Grant URF/1/4338-01-01. We also thank the
596 scientists of Taiwan that made the input data freely available.

597 **Data and codes availability statement**

598 The data and codes that support the findings of this study can be accessed at:

599 <https://doi.org/10.5281/zenodo.7005158>.

600 **Appendix A. Summary of lithology class**

Class	Description
A	Alluvium
B	Andesite, basalt, and serpentine
C	Metamorphic limestone
D	Black schist, green schist, and sandy schist
E	Laterite, gravel, sand and clay
F	Mudstone intercalated with allochthon
G	Gneiss
H	Hard shale and sandstone
I	Agglomerate and tuffaceous sandstone
J	Sandstone, mudstone, and shale
K	Phyllite, slate, and sandstone
L	Sandstone, shale, and coaly shale
M	Quartzite, slate, and coaly shale
N	Shale, siltstone, and sandstone
O	Hard shale, slate, and Phyllite

601

602 **Appendix B. Description of different sub-regions**

Sub-region ID	Description
1	New Taipei City, Taipei City, Keelung City, Taoyuan County
2	Hsinchu City, Hsinchu County
3	Yilan County
4	Miaoli County
5	Taichung City
6	Chiayi County, Chiayi City, Yunlin County, Changhua County
7	Nantou County
8	Hualien County
9	Tainan City
10	Kaohsiung City
11	Taitung County
12	Pingtung County

603

604 **References**

- 605 Aguilera, Q., Lombardo, L., Tanyas, H., Lipani, A., 2022. On the prediction of landslide occurrences and
606 sizes via Hierarchical Neural Networks. *Stoch. Env. Res. Risk. A*.
- 607 Akaike, H., 1974. A new look at the statistical model identification. *Ieee. T. Automat. Contr*, 19, 716-
608 723.
- 609 Alvioli, M. et al., 2016. Automatic delineation of geomorphological slope units with r. slopeunits v1. 0
610 and their optimization for landslide susceptibility modeling. *Geoscientific Model Development*,
611 9, 3975.
- 612 Atkinson, P.M., Massari, R., 1998. Generalised linear modelling of susceptibility to landsliding in the
613 central Apennines, Italy. *Comput. Geosci.*, 24, 373-385.
- 614 Bryce, E., Lombardo, L., van Westen, C., Tanyas, H., Castro-Camilo, D., 2022. Unified landslide hazard
615 assessment using hurdle models: a case study in the Island of Dominica. *Stoch. Env. Res. Risk.*
616 *A.*, 1-14.
- 617 Carrara, A., 1988. Drainage and Divide Networks Derived from High-Fidelity Digital Terrain Models.

618 in: Chung, C.F., Fabbri, A.G., Sinding-Larsen, R. (Eds.), *Quantitative Analysis of Mineral and*
619 *Energy Resources*. Springer Netherlands, Dordrecht, pp. 581-597.

620 Chen, C.-W. et al., 2019a. Assessing landslide characteristics in a changing climate in northern Taiwan.
621 *Catena*, 175, 263-277.

622 Chen, T.-H.K., Prishchepov, A.V., Fensholt, R., Sabel, C.E., 2019b. Detecting and monitoring long-term
623 landslides in urbanized areas with nighttime light data and multi-seasonal Landsat imagery
624 across Taiwan from 1998 to 2017. *Remote Sens. Environ.*, 225, 317-327.

625 Chung, C.-J.F., Fabbri, A.G., Westen, C.J.V., 1995. Multivariate regression analysis for landslide hazard
626 zonation, *Geographical information systems in assessing natural hazards*. Springer, pp. 107-133.

627 Corominas, J. et al., 2014. Recommendations for the quantitative analysis of landslide risk. *Bull. Eng.*
628 *Geol. Environ.*, 73, 209-263.

629 Emberson, R., Kirschbaum, D.B., Amatya, P., Tanyas, H., Marc, O., 2022. Insights from the topographic
630 characteristics of a large global catalog of rainfall-induced landslide event inventories. *Nat.*
631 *Hazards Earth Syst. Sci.*, 22, 1129-1149.

632 Fang, Z., Wang, Y., Peng, L., Hong, H., 2021. A comparative study of heterogeneous ensemble-learning
633 techniques for landslide susceptibility mapping. *Int. J. Geogr. Inf. Sci.*, 35, 321-347.

634 Fang, Z., Wang, Y., van Westen, C.J., Lombardo, L., 2022. Space-time landslide susceptibility modelling
635 in Taiwan.

636 Fell, R. et al., 2008. Guidelines for landslide susceptibility, hazard and risk zoning for land use planning.
637 *Eng. Geol.*, 102, 85-98.

638 Gariano, S.L., Guzzetti, F., 2016. Landslides in a changing climate. *Earth-sci. Rev.*, 162, 227-252.

639 Goetz, J.N., Guthrie, R.H., Brenning, A., 2011. Integrating physical and empirical landslide susceptibility
640 models using generalized additive models. *Geomorphology*, 129, 376-386.

641 Guzzetti, F., Carrara, A., Cardinali, M., Reichenbach, P., 1999. Landslide hazard evaluation: a review of
642 current techniques and their application in a multi-scale study, Central Italy. *Geomorphology*,
643 31, 181-216.

644 Guzzetti, F., Malamud, B.D., Turcotte, D.L., Reichenbach, P., 2002. Power-law correlations of landslide
645 areas in central Italy. *Earth. Planet. Sc. Lett*, 195, 169-183.

646 Guzzetti, F. et al., 2012. Landslide inventory maps: New tools for an old problem. *Earth-sci. Rev.*, 112,
647 42-66.

648 Guzzetti, F., Reichenbach, P., Cardinali, M., Galli, M., Ardizzone, F., 2005. Probabilistic landslide
649 hazard assessment at the basin scale. *Geomorphology*, 72, 272-299.

650 Hung, J.-J., 2000. Chi-Chi earthquake induced landslides in Taiwan. *Earthquake Engineering and*
651 *Engineering Seismology*, 2, 25-33.

652 Jaiswal, P., van Westen, C.J., Jetten, V., 2010. Quantitative landslide hazard assessment along a
653 transportation corridor in southern India. *Eng. Geol.*, 116, 236-250.

654 Jones, J.N., Boulton, S.J., Stokes, M., Bennett, G.L., Whitworth, M.R., 2021. 30-year record of Himalaya
655 mass-wasting reveals landscape perturbations by extreme events. *Nat. Commun.*, 12, 1-15.

656 Katz, O., Morgan, J.K., Aharonov, E., Dugan, B., 2014. Controls on the size and geometry of landslides:
657 Insights from discrete element numerical simulations. *Geomorphology*, 220, 104-113.

658 Lee, C.-T., 2013. Re-evaluation of factors controlling landslides triggered by the 1999 Chi-Chi
659 earthquake, *Earthquake-induced landslides*. Springer, pp. 213-224.

660 Lin, C.-W. et al., 2011. Landslides triggered by the 7 August 2009 Typhoon Morakot in southern Taiwan.
661 *Eng. Geol.*, 123, 3-12.

662 Lin, E., Liu, C., Chang, C., Cheng, I., Ko, M., 2013. Using the formosat-2 high spatial and temporal
663 resolution multispectral image for analysis and interpretation landslide disasters in taiwan. *J.*
664 *Photogramm. Remote Sens.*, 17, 31-51.

665 Lombardo, L. et al., 2019. Geostatistical modeling to capture seismic-shaking patterns from earthquake-
666 induced landslides. *Journal of Geophysical Research: Earth Surface*, 124, 1958-1980.

667 Lombardo, L., Opitz, T., Ardizzone, F., Guzzetti, F., Huser, R., 2020. Space-time landslide predictive
668 modelling. *Earth-sci. Rev.*, 103318.

669 Lombardo, L., Opitz, T., Huser, R., 2018. Point process-based modeling of multiple debris flow
670 landslides using INLA: an application to the 2009 Messina disaster. *Stoch. Env. Res. Risk. A.*,
671 32, 2179-2198.

672 Lombardo, L., Tanyas, H., 2021. From scenario-based seismic hazard to scenario-based landslide hazard:
673 fast-forwarding to the future via statistical simulations. *Stoch. Env. Res. Risk. A.*, 1-14.

674 Lombardo, L., Tanyas, H., Huser, R., Guzzetti, F., Castro-Camilo, D., 2021. Landslide size matters: A
675 new data-driven, spatial prototype. *Eng. Geol.*, 106288.

676 Malamud, B.D., Turcotte, D.L., Guzzetti, F., Reichenbach, P., 2004. Landslide inventories and their
677 statistical properties. *Earth. Surf. Proc. Land*, 29, 687-711.

678 Medwedeff, W.G., Clark, M.K., Zekkos, D., West, A.J., 2020. Characteristic landslide distributions: An
679 investigation of landscape controls on landslide size. *Earth. Planet. Sc. Lett.*, 539, 116203.
680 Merghadi, A. et al., 2020. Machine learning methods for landslide susceptibility studies: A comparative
681 overview of algorithm performance. *Earth-sci. Rev.*, 2020, 103225.
682 Monsieurs, E., Dewitte, O., Demoulin, A., 2019. A susceptibility-based rainfall threshold approach for
683 landslide occurrence. *Nat. Hazards Earth Syst. Sci.*, 19, 775-789.
684 Moreno, M., Steger, S., Tanyas, H., Lombardo, L., 2022. Modeling the size of co-seismic landslides via
685 data-driven models: the Kaikōura's example.
686 Nandi, A., Shakoor, A., 2010. A GIS-based landslide susceptibility evaluation using bivariate and
687 multivariate statistical analyses. *Eng. Geol.*, 110, 11-20.
688 Nefeslioglu, H.A., Gorum, T., 2020. The use of landslide hazard maps to determine mitigation priorities
689 in a dam reservoir and its protection area. *Land Use Policy*, 91, 104363.
690 Nowicki Jessee, M.A. et al., 2018. A Global Empirical Model for Near-Real-Time Assessment of
691 Seismically Induced Landslides. *Journal of Geophysical Research: Earth Surface*, 123, 1835-
692 1859.
693 Ohlmacher, G.C., 2007. Plan curvature and landslide probability in regions dominated by earth flows
694 and earth slides. *Eng. Geol.*, 91, 117-134.
695 Opitz, T., Bakka, H., Huser, R., Lombardo, L., 2022. High-resolution Bayesian mapping of landslide
696 hazard with unobserved trigger event. *The Annals of Applied Statistics*, 16, 1653-1675.
697 Park, J.-Y., Lee, S.-R., Lee, D.-H., Kim, Y.-T., Lee, J.-S., 2019. A regional-scale landslide early warning
698 methodology applying statistical and physically based approaches in sequence. *Eng. Geol.*, 260,
699 105193.
700 Reichenbach, P., Rossi, M., Malamud, B., Mihir, M., Guzzetti, F., 2018. A review of statistically-based
701 landslide susceptibility models. *Earth-sci. Rev.*, 180, 60-91.
702 Rossi, M. et al., 2019. A predictive model of societal landslide risk in Italy. *Earth-sci. Rev.*, 196, 102849.
703 Schwarz, M., Preti, F., Giadrossich, F., Lehmann, P., Or, D., 2010. Quantifying the role of vegetation in
704 slope stability: A case study in Tuscany (Italy). *Ecol. Eng.*, 36, 285-291.
705 Segoni, S., Piciullo, L., Gariano, S.L., 2018. A review of the recent literature on rainfall thresholds for
706 landslide occurrence. *Landslides*, 15, 1483-1501.
707 Steger, S., Brenning, A., Bell, R., Glade, T., 2017. The influence of systematically incomplete shallow
708 landslide inventories on statistical susceptibility models and suggestions for improvements.
709 *Landslides*, 14, 1767-1781.
710 Steger, S., Brenning, A., Bell, R., Petschko, H., Glade, T., 2016. Exploring discrepancies between
711 quantitative validation results and the geomorphic plausibility of statistical landslide
712 susceptibility maps. *Geomorphology*, 262, 8-23.
713 Stepinski, T.F., Jasiewicz, J., 2011. Geomorphons-a new approach to classification of landforms.
714 *Proceedings of geomorphometry*, 2011, 109-112.
715 Tanyaş, H., Allstadt, K.E., van Westen, C.J., 2018. An updated method for estimating landslide-event
716 magnitude. *Earth. Surf. Proc. Land*, 43, 1836-1847.
717 Tanyaş, H., Hill, K., Mahoney, L., Fadel, I., Lombardo, L., 2022. The world's second-largest, recorded
718 landslide event: Lessons learnt from the landslides triggered during and after the 2018 Mw 7.5
719 Papua New Guinea earthquake. *Eng. Geol.*, 297, 106504.
720 Titti, G., van Westen, C., Borgatti, L., Pasuto, A., Lombardo, L., 2021. When Enough Is Really Enough?
721 On the Minimum Number of Landslides to Build Reliable Susceptibility Models. *Geosciences*,
722 11, 469.
723 Van den Bout, B., Lombardo, L., Chiyang, M., van Westen, C., Jetten, V., 2021. Physically-based
724 catchment-scale prediction of slope failure volume and geometry. *Eng. Geol.*, 284, 105942.
725 Van Westen, C., Rengers, N., Soeters, R., 2003. Use of geomorphological information in indirect
726 landslide susceptibility assessment. *Nat. Hazards*, 30, 399-419.
727 Varnes, D.J., 1984. *Landslide hazard zonation: a review of principles and practice*. UNESCO Press, Paris,
728 63 pp.
729 Wang, N. et al., 2022. Space-time susceptibility modeling of hydro-morphological processes at the
730 Chinese national scale. *Eng. Geol.*, 301, 106586.
731 Wang, N. et al., 2021. Using satellite rainfall products to assess the triggering conditions for hydro-
732 morphological processes in different geomorphological settings in China. *International Journal of
733 Applied Earth Observation and Geoinformation*, 102, 102350.
734 Wood, S.N., 2006. *Generalized additive models: an introduction with R*. Chapman and Hall/CRC.
735 Wood, S.N., 2011. Fast stable restricted maximum likelihood and marginal likelihood estimation of
736 semiparametric generalized linear models. *Journal of the Royal Statistical Society: Series B
737 (Statistical Methodology)*, 73, 3-36.

738 Wu, C.-H., Chen, S.-C., 2009. Determining landslide susceptibility in Central Taiwan from rainfall and
739 six site factors using the analytical hierarchy process method. *Geomorphology*, 112, 190-204.
740 Yang, C.-J., Turowski, J.M., Hovius, N., Lin, J.-C., Chang, K.-J., 2021. Badland landscape response to
741 individual geomorphic events. *Nat. Commun.*, 12, 4631.
742 Zhang, J. et al., 2019. How size and trigger matter: analyzing rainfall-and earthquake-triggered landslide
743 inventories and their causal relation in the Koshi River basin, central Himalaya. *Nat. Hazards*
744 *Earth Syst. Sci.*, 19, 1789-1805.

745

746